

# Route to localising elastic energy via the topological rainbow effect

Bogdan Ungureanu<sup>1</sup>, Mehul P. Makwana<sup>1,2</sup>, Richard V. Craster<sup>1,3,4</sup>, Sébastien Guenneau<sup>4</sup>

<sup>1</sup> *Department of Mathematics, Imperial College London, London SW7 2AZ, United Kingdom*

<sup>2</sup> *Multiwave Technologies AG, 3 Chemin du Pré Fleuri, 1228, Geneva, Switzerland*

<sup>3</sup> *Department of Mechanical Engineering, Imperial College London, London SW7 2AZ, United Kingdom and*

<sup>4</sup> *UMI 2004 Abraham de Moivre-CNRS, Imperial College London, SW7 2AZ, United Kingdom*

We combine three different fields, topological physics, metamaterials and elasticity to design a topological metasurface to control and redirect elastic waves. We strategically design a two-dimensional crystalline perforated elastic plate, that hosts symmetry-induced topological edge states. By concurrently allowing the elastic substrate to spatially vary in depth, we are able to convert the incident flexural wave into a series of robust modes, with differing envelope modulations. This adiabatic transition localises the incoming elastic energy into a concentrated region where it can then be damped or extracted. This elastic “topological rainbow” effect leverages two main concepts, namely the quantum valley-Hall effect and the rainbow effect usually associated with electromagnetic metamaterials. Due to the directional tunability of the elastic energy by geometry our results have far-reaching implications for mechanical vibration applications such as switches, filters and energy-harvesters.

## I. INTRODUCTION

A fundamental theme in wave physics is the influence of local material, or geometrical, structurations on the global propagative behaviour of waves through a medium. A crucial feature of periodic structures is that they exhibit Bragg scattering and interference that has, subsequently, led to the fields of photonic crystals [1, 2] and crystal fibers [3, 4] in optics and phononic crystals [5, 6] in acoustics. An extension of using geometry, for wave propagation, is to draw upon the budding field of topological insulators [7–9] and develop topological photonic devices to guide and confine wave energy. Recent developments, within this field, allow us to a priori identify strategic symmetries that, when broken, lead to topologically nontrivial band gaps in which robust edge states are guaranteed to reside.

There are two canonical types of topological insulators, those which preserve time-reversal symmetry (TRS) and those which do not. For the former, quantum systems utilise the orthogonality between  $\pm$  spin-1/2 fermionic particles to ensure backscattering immunity. This property cannot be used by Newtonian systems that solely consist of spin-1 bosonic-like particles. In order to bridge the gap, between quantum and continuum mechanics, we take advantage of the pseudospins, inherent within certain Newtonian structures, and use them as an analogue for fermionic spins. By gapping a pair of TRS related Dirac cones, two “valleys” (regions of locally quadratic curvature) are created. The pair of eigensolutions, associated with each of these valleys, are themselves endowed with their own designated pseudospin. Hence, this binary valley degree of freedom can be used to design valleytronic devices similar to those in spintronics by leveraging the valley pseudospin in the manner of electron spin [10–19]. The inhibition of backscattering is reliant upon there being no intervalley scattering, hence, the valley-Hall effect of our proposed system requires a careful tuning of the system and geometrical parameters [20]. Despite this, these passive valley-Hall systems simply rely upon the breaking of spatial symmetries to induce quasi-topological modes and are therefore, from a practical perspective, more straightforward to realise.

Although Newtonian systems do not afford us the same degrees of freedom as quantum systems; transposing and extending concepts from topological insulators to elastic vibrations remains naturally attractive [17, 18, 21–23]. Structured elastic plate models are the primary avenue for accessing elastic problems for physicists; as such they have been, and will continue to be, the fundamental model studied. Here we systematically engineer, a perforated elastic plate, such that it admits symmetry-induced topological states. The plate dimensions, elastic parameters and wave frequencies used are illustrative for thin soil layers in geophysics and civil engineering [24–28].

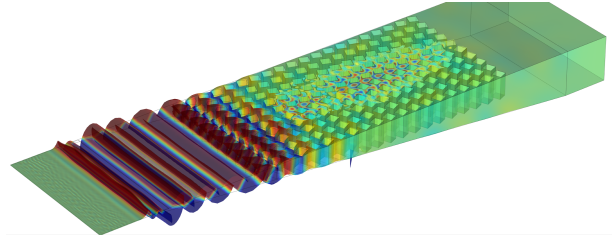


Figure 1: A rightward incident flexural plane-wave encounters a large crystal composed of a geometrical arrangement of square holes; this crystal is split into two halves to create an interface along which a valley-Hall edge state propagates. The spatial grading in thickness then gradually slows the edge wave allowing for the concentration of elastic energy.

Previous work in civil engineering [29], which introduces an elastic metasurface created by a graded metawedge of resonators that alter in height, has acted as an inspiration for our current model. The metawedge creates a device that allows for the mode conversion of surface Rayleigh waves into mainly harmless downward propagating shear bulk waves, or into a frequency selective surface where different frequency components are concentrated at different positions; the metawedge used in [29] is, in turn, motivated by the optical rainbow effect that was proposed over a decade ago [30]. There, the authors used a graded wedge of subwavelength resonators to

trap and spatially segregate the different frequencies of light. In elasticity, similar principles have also been used to demonstrate how an array of graded resonators buried in the soil can act as a seismic barrier [31]. The principle of light, sound and elastic wave trapping via graded metasurfaces [32–37] is markedly different from that achieved in elastic plates structured with sub-wavelength resonating beams [38], which is based on insertion of defects or randomization.

In this article we effectively combine the planar valley-Hall effect with the rainbow effect. The latter effect is contingent upon the spatial grading in depth, whilst the presence of topological modes relies upon the planar arrangement of the perforations (see Fig. 1). Using this model, we demonstrate how a flexural source couples into a symmetry-induced topological edge state before becoming localised at a specific location within the crystal.

## II. FORMULATION

The time-harmonic Navier’s equations, which govern the total displacement through an elastic medium, are written as,

$$\nabla \cdot [\mathbb{C} : \nabla \mathbf{u}] + \rho \omega^2 \mathbf{u} = \mathbf{0}, \quad (1)$$

where we have excluded a source term (typically a line force to generate a plane flexural wave as shown in Fig. 1, or a point force), the displacement  $\mathbf{u}(\mathbf{x}) = (u_1(\mathbf{x}), u_2(\mathbf{x}), u_3(\mathbf{x}))$ ,  $\mathbf{x} = (x_1, x_2, x_3)$  and  $\mathbb{C}$  is the rank-4 (symmetric) elasticity tensor with entries  $C_{ijkl} = \lambda \delta_{ij} \delta_{kl} + \mu (\delta_{ik} \delta_{jl} + \delta_{il} \delta_{jk})$ ,  $i, j, k, l = 1, 2, 3$ , i.e. isotropic,  $\lambda$  and  $\mu$  being the Lamé parameters,  $\rho$  the mass density and  $\omega$  the angular frequency of the wave.

We set stress-free boundary conditions at all interfaces with air:

$$(\mathbb{C} : \nabla \mathbf{u}) \cdot \mathbf{n} = (\mathbb{C} : \epsilon(\mathbf{u})) \cdot \mathbf{n} = \mathbf{0} \quad (2)$$

where  $\epsilon(\mathbf{u})$  is the rank-2 strain tensor with entries  $\epsilon_{ij} = 1/2 (\partial u_i / \partial x_j + \partial u_j / \partial x_i)$  and  $\mathbf{n}$  is the outward pointing normal to the boundaries. We solve the weak form of equation (1) using the commercial finite element software COMSOL [39].

To model an unbounded domain, within our bounded system, we utilise Perfectly Matched Layers (PMLs) to strongly absorb incoming waves in a reflectionless manner. Notably, our problem becomes especially challenging for our 3D plate configuration (see Fig. 1) when considering a point force. Here we require PMLs to impose the zero elastic displacement-vector field condition along the entire outer boundary of the computational domain. We use adaptative elastic PMLs, which are well suited for dealing with cases, ranging from the quasi-static limit to high-frequency settings, and are obtained from Navier equations (1), using the transformation [40],

$$(x'_1, x'_2, x'_3) = \left( \int_0^{x_1} s_1(\xi) d\xi, \int_0^{x_2} s_2(\xi) d\xi, \int_0^{x_3} s_3(\xi) d\xi \right).$$

The  $(x'_1, x'_2, x'_3)$  are the working complex coordinates and the stretches  $s_1(\xi), s_2(\xi), s_3(\xi)$  are either equal to 1 or to  $(\xi/L) (1 - i)G$ , depending on the direction along which one would like to absorb the wave; in our plate configuration, we set  $s_3(\xi) = 1$ . The width of the PML region  $L$  is a geometrical parameter that is automatically extracted from each region, whereas, the dimensionless PMLs scaling factor  $G$  can be modified at will in order to achieve the needed PML efficiency [40].

For band structure calculations, we take advantage of the periodicity of the system in the horizontal  $x_1 - x_2$ -plane, and consider a single elementary cell and imagine an infinite crystal. We look for Floquet-Bloch eigensolutions in the form

$$\mathbf{u}(x_1 + d, x_2 + d, x_3) = \mathbf{u}_{\boldsymbol{\kappa}}(x_1, x_2, x_3) \exp(i(\kappa_1 d + \kappa_2 d)) \quad (3)$$

where  $\boldsymbol{\kappa} = (\kappa_1, \kappa_2)$  is the Bloch vector which is evaluated within and on the first Brillouin zone (BZ) (see Fig. 2) and  $d$  is the pitch of the lattice.

## III. ENGINEERING TOPOLOGICAL EDGE STATES USING A $C_{4v}$ CELLULAR STRUCTURE

Many attractive phenomena associated with valley contrasting properties have been predicted and experimentally observed, such as valley filters and valley-Hall effects [10–19]. Dirac cones are degeneracies in the Bloch spectrum, whose presence, are a prerequisite for whether or not these valley-Hall edge states are obtainable. Dirac cones broadly fall into three categories: symmetry-induced (as in graphene), non-symmetry repelled (as we have here) and purely accidental. We have veered away from the majority of the literature in this field by considering a carefully engineered structure that hosts non-symmetry repelled Dirac cones in a square lattice. The square structure has been shown to possess many unique properties that are not ordinarily exhibited within the canonical graphene-like structures e.g. three-way partitioning of energy, topological transport around a  $\pi/2$  bend [41–43]. The valley-Hall effect arises from the gapping of a pair of Dirac cones (not necessarily symmetry-induced) and these result in nontrivial band gaps where broadband edge states are guaranteed to reside. The topological invariant that dictates the construction of our neighboring media is the valley-Chern number [44]; this takes nonzero values locally at the TRS related valleys. By attaching two media with opposite valley-Chern numbers, broadband valley-Hall edge states arise. If a source is placed along an interface, that partitions two topologically distinct regions, a zero-line mode (ZLM) will be excited.

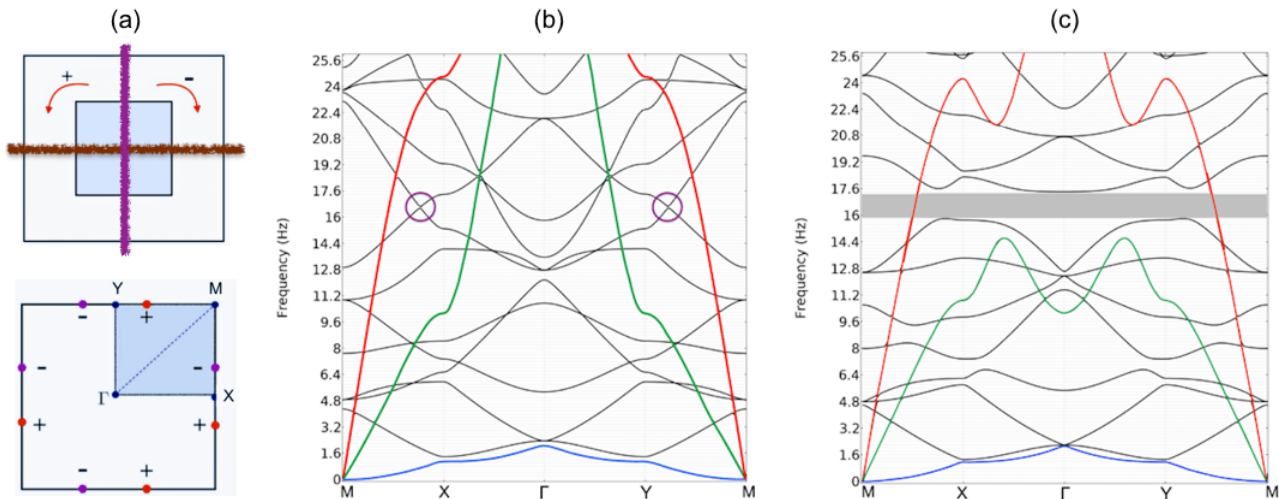


Figure 2: Physical space structure in the upper panel of (a) shows our cellular geometry. The Floquet-Bloch band diagram in (b) is associated with the cellular structure, that consists of an unrotated inclusion, and that possesses, both, vertical and horizontal reflectional symmetries. Dispersion curves in (c) arise from either, a positively or negatively, rotated internal inclusion. The lower BZ plot in (a) highlights the region, in which the dispersion curves are plotted around, as well as the regions of inequivalent nonzero valley-Chern numbers that lead to the generation of the valley-Hall edge states [45]. Panels (b) and (c) are for all 3 polarizations of elastic waves propagating within a periodically perforated soil plate (density  $1800 \text{ [kg/m}^3\text{]}$ , Young's modulus  $0.15^9 \text{ [Pa]}$ , Poisson's ratio 0.20) 10 cm in thickness with stress-free air perforations ( $2\text{m} \times 2\text{m}$ ) in a square array of pitch 3m; the lowest bands are for out-of-plane flexural waves (blue), and in-plane shear (green) and pressure (red) waves. All black curves are primarily of flexural polarization. Note the presence of Dirac points at frequency 16.60 Hz in (b) that are then absent in (c). The topologically nontrivial band gap that is opened, between the frequencies 15.8 – 17 Hz, will host the symmetry-induced edge states.

In this article, we opt to utilise the non-symmetry repelled Dirac cones present within a cellular structure that possesses a  $C_{4v}$  point group symmetry, Fig. 2(a). We chose this structure, over the hexagonal  $C_{6v}$  canonical counterpart, due to the longer-envelope modulation present with the resulting edge states [41]; the benefits of this will become evident in Sec. IV. The unrotated cellular structure chosen, Fig. 2(a), contains, both, horizontal and vertical mirror symmetries along with four-fold rotational symmetry. Notably, it is the presence of these mirror symmetries that allows for a conical intersection to manifest itself via parametric variation in our system (1) (see [41, 42] for further details). From Fig. 2(b) it is evident that, for our structured elastic plate of depth 10cm, the Dirac cones are located at  $\omega/2\pi = 16.60 \text{ Hz}$ .

By rotating the internal square perforation by 22.5 degrees, both mirror symmetries are broken, yielding a band gap that ranges between  $\omega/2\pi = 15 - 17.6 \text{ Hz}$ , Fig. 2(b). Notably, this band gap exists for both, flexural waves and in-plane shear waves; also note that the in-plane pressure waves are irrelevant for us as our sole focus is on the control of flexural waves. In Fig. 2(c) we see a pair of well-defined extrema (i.e. valleys) along the  $MX$  and  $YM$  boundary paths of the BZ, which are separated by an omnidirectional band gap. These valleys are locally imbued with a quantized topological charge which is defined as the signum of the valley-Chern number [43]; this quantized quantity is system-independent and shown as an overlay, of the BZ, in Fig. 2(b). Importantly,

for topologically inequivalent states, the chirality is reversed due to the presence of TRS [10–19].

We generate ZLMs, for an elastic plate of constant depth, by placing one gapped medium above its reflectional twin, see Fig. 3. The simplicity of this construction, the added protection afforded by the imbued chirality and the a priori knowledge of how to tessellate the two media, to produce these broadband edge states, is the main benefit of these geometrically engineered modes. The topological protection afforded by these valley-Hall states, when we apply a sufficiently small perturbation, is attributed to the orthogonality of the pseudospins. Fig. 3(a), shows how even and odd-parity edge states exist along an interface that separates oppositely perturbed media; the edge states drawn here reside in the band gap frequency range of Fig. 2(c). The regions that demarcate the band gap in Fig. 2(c), and that have locally quadratic curvature, are precisely the regions of opposite  $\pm$  pseudospins shown in Fig. 3(a).

Fig. 3(b) shows a scattering computation for an ungraded elastic medium, whose planar symmetries are those of the ribbons shown in Fig. 3(a), albeit extended in the longitudinal direction. Here a flexural even-parity edge wave is excited at  $\omega/2\pi = 17 \text{ Hz}$  via an incident plane-wave source. We reiterate that a pleasant feature of these states is that they are reliant upon a simple passive symmetry-based construction and hence they provide a practical means to guide flexural

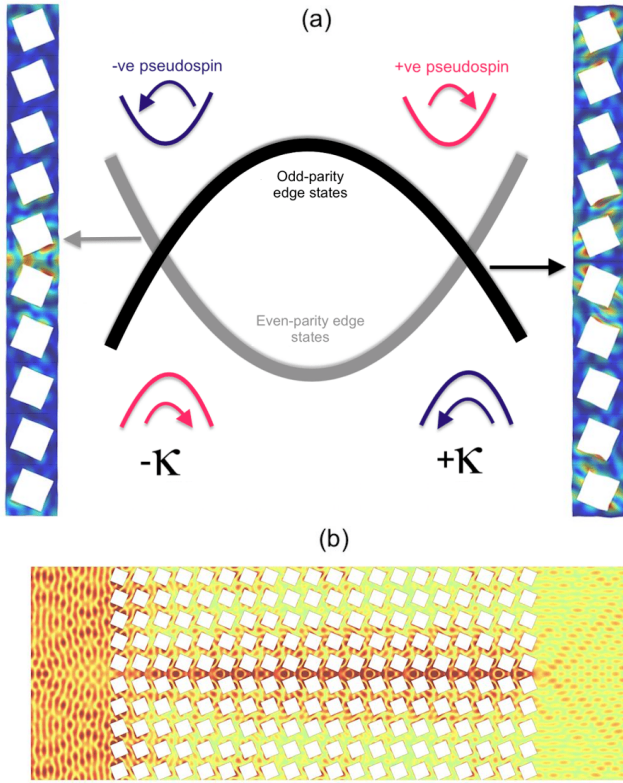


Figure 3: Panel (a) illustrates the opposite parity edge states that exist within the band gap frequency range of the bulk medium. The even and odd-parity eigenmodes exist at the frequencies,  $\omega/(2\pi) = 16.5, 16.55$  Hz, respectively. The two ribbon eigenmodes shown depict the absolute values of the out-of-plane components of the modes propagating along the interface between oppositely orientated squares. Periodic boundary conditions have been applied to left and right-side of this ribbon with Floquet-Bloch conditions applied along the top and bottom boundaries. Panel (b) shows how an even-parity flexural edge state is excited, in an elastic plate of constant thickness (10cm), by a left-incident plane-wave at the frequency  $\omega/(2\pi) = 16.5$  Hz.

waves, for frequencies below 20 Hz, in a pragmatic elastic plate model.

#### IV. TOPOLOGICAL RAINBOW EFFECT

We have routinely seen how symmetry-induced topological edge states behave along interfaces [10–16], around different angled bends [17, 23] and within topological circuits [18, 41], for a myriad of Newtonian systems. However we have yet to see how these planar states behave when they are incorporated in a medium that grades in depth; this is precisely the phenomena that we explore in this section.

#### A. Slow wave elastic energy concentration using a topological wedge

The elastic plate ZLM, for a substrate of constant depth, in Fig. 3(b) is solely due to the spatial symmetries in the two-dimensional plane. By using the additional depth degree of freedom, as we have in the elastic substrate shown in Fig. 4(a), we arrive at a significantly different excitation pattern, Fig. 4(d). The localised patch of energy, furthest to the right of the crystal, is a symptom of the adiabatic grading. As the depth of the elastic medium increases, the one-dimensional dispersion curves shift *upwards*. Hence, for a fixed frequency source, the mode excited progressively gets closer to becoming a standing wave as it moves along the domain wall, Fig. 4(b). This concentration of slow edge wave energy has the potential to then be damped or extracted for energy-harvesting purposes.

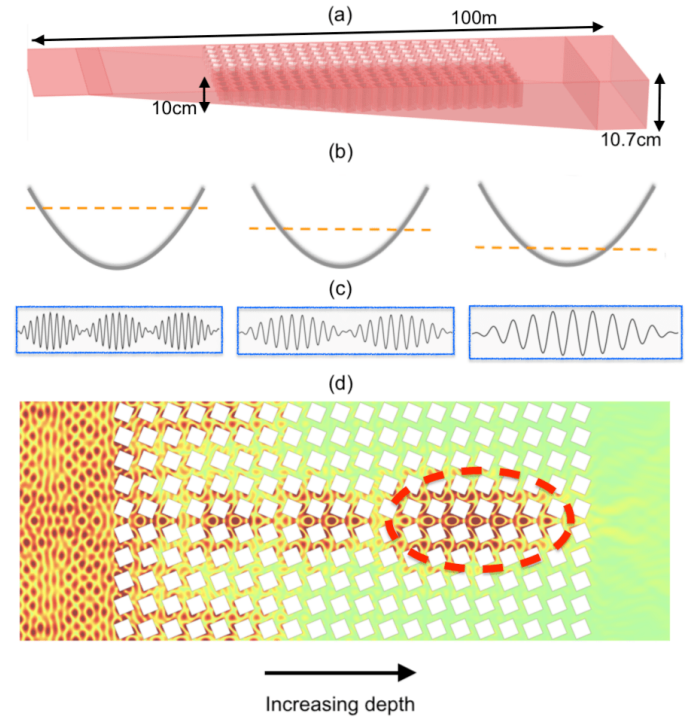


Figure 4: Panel (a) shows the periodically perforated soil plate that varies in depth (from 10cm to 10.7cm). By sending in a plane-wave source of fixed frequency  $\omega/2\pi = 17.3$  Hz, the rightward mode excited shifts its position along the even-parity dispersion curve (shown in Fig. 3(a)). Importantly, as the depth of the elastic substrate increases, the curve shifts upwards (black solid line) whilst the excitation frequency (orange dashed line) remains unchanged. As the modal excitation approaches the standing wave at  $\Gamma$  the period of the envelope modulation decreases as shown in (c). The magnitude of the out-of-plane component of the displacement is shown in panel (d); the region of concentrated energy is highlighted by the red dashed circle.

Note that the envelope modulation also adiabatically

changes, alongside the depth change, Fig. 4(c). As the ZLM approaches the standing wave frequency the period of the envelope modulation increases. Since the valley-Hall state is a weak topological state protected solely by symmetry, care must be taken to prohibit backscattering hence knowledge of the long-scale envelope is especially useful for finite length interfaces as it can be used to minimise reflections. The inhibition of backscattering inherent within topological modes differentiates us from earlier articles that have utilised an adiabatic grading [46]. An asymptotic method, more commonly known as high-frequency homogenisation (HFH) allows for the characterisation of this long-scale envelope [47, 48]. The Fourier separation between counter-propagating edge states is highly relevant to the transmission properties of the topological guide [18]. The Fourier separation for canonical hexagonal structures is greater than that of our  $C_{4v}$  structure; this is due to the Dirac cones occurring precisely at the high-symmetry points of the BZ for the former but not for the latter. The smaller Fourier separation for our model has two effects on our system, as shown in Fig. 4. Firstly the initial mode excited, at the start of the crystal, has a discernible long-scale envelope and secondly, only a small adiabatic grading in depth (0.7cm in Fig. 4) is needed to obtain a concentrated region of localised elastic energy.

If we now allow frequencies to vary, along with the linear variation in depth, we obtain the series of displacements shown in Fig. 5. Significantly, for higher frequencies the ZLM propagates further along the domain wall, before approaching a standing wave frequency. The concentrated region of elastic energy, lies further to the right of the structured elastic plate, for higher frequencies. This can be explained pictorially by Fig. 4(b); the higher the frequency, the further away the rightward propagating mode is from the standing wave and therefore a greater change in depth is needed to get this mode to adiabatically transition into a (pseudo) standing wave.

If in Fig. 4, instead of a rightward propagating plane-wave source that impacts the crystal from the left-hand side, we had a leftward propagating plane-wave impacting the crystal on the right-hand side we would obtain a starkly different displacement pattern. If, the frequency of excitation (17.3Hz) and the model was that of Fig. 4, then the mode excited would be closer to a standing wave and therefore resemble the out-of-plane displacement shown in Fig. 5(a) (albeit the localised region of nonzero displacement would be on the right-hand side of the crystal). This source dependent asymmetry in displacements is a symptom, of the broken mirror-plane symmetry, that arises from the variation in depth of our elastic substrate. For an elastic medium with constant depth, this mirror-plane symmetry is still intact, therefore this source dependent asymmetry in displacements is (almost) non-existent.

### B. Elastic edge waves to chirality-locked beam splitting

A fascinating chiral beaming phenomenon has been observed for classical and electronic valley-Hall systems [12, 49]. By exciting a valley-Hall crystal near the periphery of the topological band gap (Fig. 4) we enable a spatial separation of

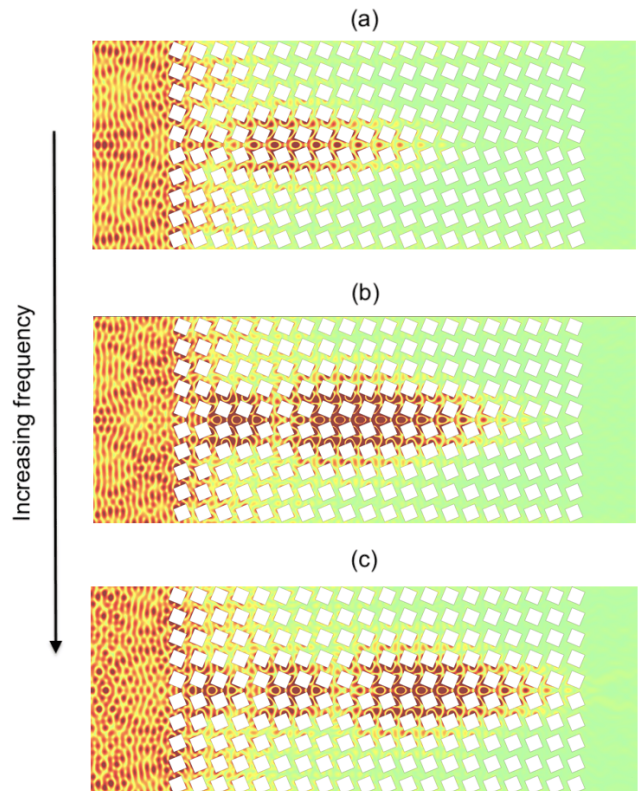


Figure 5: Displacement fields, for the model in Fig. 4, are shown here for three other frequencies,  $\omega/2\pi = 17\text{Hz}, 17.1\text{Hz}, 17.2\text{Hz}$  (top to bottom). Notably, as the frequencies increase, the region of concentrated elastic energy, shifts further to the right. This is due to the topological mode, that is initially excited by the incident plane-wave, being further away, from the standing wave at  $\Gamma$ , for higher frequencies.

vortex states that carry opposite pseudospins or chirality. This phenomenon is especially meaningful in systems that do not have an intrinsic spin polarization.

This effect is induced adiabatically, in our elastic system, by increasing the depth variation. The elastic substrate in Fig. 6 now ranges from 10cm to 12cm as opposed to the 0.7cm variation shown in Fig. 4. Due to the greater variation in depth the modal excitation shifts, more dramatically (see Fig. 6(b)), than in Fig. 4(b). Therefore, a topological ZLM is initially triggered before it transitions into a pair of pseudospin-locked beams, Fig. 6(b). The excitation of the  $\pi/3$  separated  $\pm$  pseudospin states stems from the gradient direction of the triangular isofrequency contours [12, 49].

### V. CONCLUSION

We have combined the rainbow effect [30, 50, 51], with a symmetry-induced topological insulator, to demonstrate the elastic *topological rainbow effect* for low-frequency surface elastic waves. By combining these two phenomena, a ro-

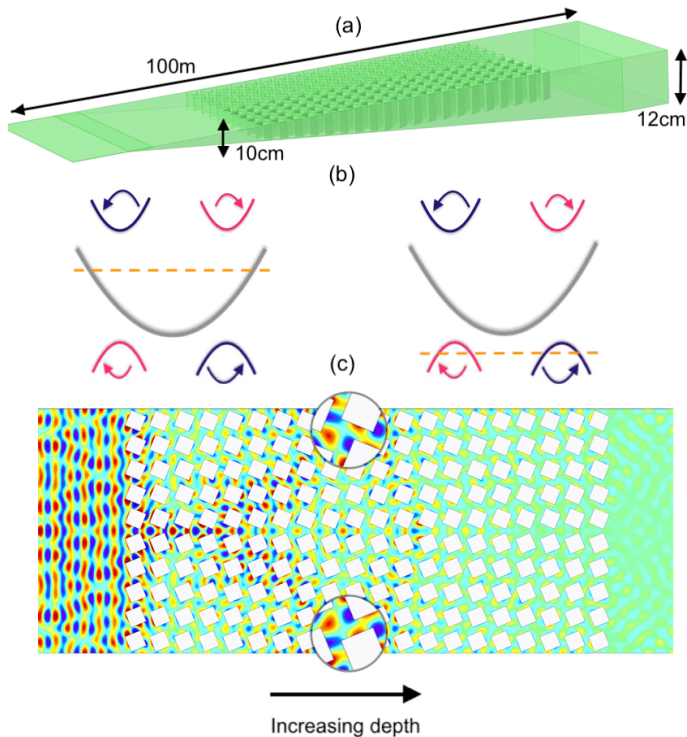


Figure 6: Panel (a) shows the dimensions of our elastic substrate. Note the enhanced depth variation when compared to Fig. 4. The Fourier space manifestation of this change is shown in (b). The mode excited by the source ( $\omega/2\pi = 16.75\text{Hz}$ ) drastically shifts into the vortex band edge modes that induces the chirality-locked beam splitting shown in (c). For clarity we have opted to plot the real component of the out-of-plane displacement in (c). Magnifications of the two oppositely polarized beams are shown to emphasise their  $\pi/3$  separation.

bust elastic edge state smoothly transitions into, either, a localised standing wave or a pair of chirality-locked beams. We have demonstrated this using detailed finite element simulations which solved the full 3D vector Navier system. Note that our design is generic and transposable to a myriad of different regimes; for example, they could be scaled up or down and the elastic parameters adapted to achieve similar adiabatic behaviours for ultrasonics [46]. Similar effects would also be achievable if we opted to use clamped holes in place of stress-free holes. The former are good models for clamped seismic metamaterials which offer a promising route to seismic protection [52]. We emphasise that the model used herein is only an approximate model for Rayleigh waves in soil substrates as the granular nature of the soil brings additional features into play [53]. Finally, the design paradigm espoused herein is generic and expected to function in a similar manner for other geometries that yield valley-Hall edge states. We hope that this study serves as a starting point for the utilisation of topological modes in energy concentration and harvesting applications [54].

#### ACKNOWLEDGMENTS

Bogdan Ungureanu acknowledges funding of European Union (MARIE SKODOWSKA-CURIE ACTIONS project Acronym/Full Title: METAQUAKENG - Metamaterials in Earthquake Engineering - MSCA IF - H2020). Richard Craster and Mehul Makwana thank the UK EPSRC for their support through grants EP/L024926/1 and EP/T002654/1.

- 
- [1] E. Yablonovitch, *Phys. Rev. Lett.* (1987).
  - [2] J. D. Joannopoulos, S. G. Johnson, J. N. Winn, and R. D. Meade, *Photonic Crystals, Molding the Flow of Light*, 2nd ed. (Princeton University Press, Princeton, 2008).
  - [3] J. Knight, T. A. Birks, P. Russell, and D. Atkin, *Optics Letters* **21**, 1547 (1996).
  - [4] F. Zolla, G. Renversez, A. Nicolet, B. Kuhlmeiy, S. Guenneau, and D. Felbacq, *Foundations of photonic crystal fibres* (Imperial College Press, London, 2005).
  - [5] M. S. Kushwaha, P. Halevi, L. Dobrzynski, and B. Djafari-Rouhani, *Phys. Rev. Lett.* **71**, 2022 (1993).
  - [6] V. Laude, *Phononic crystals: Artificial Crystals for Sonic, Acoustic, and Elastic Waves* (DeGruyter, Berlin/Boston, 2015).
  - [7] C. L. Kane and E. J. Mele, *Physical Review Letters* **95**, 146802 (2005).
  - [8] M. Z. Hasan and C. L. Kane, *Rev. Mod. Phys.* **82**, 3045 (2010).
  - [9] D. Xiao, W. Yao, and Qian Niu, *Physical Review Letters* **99**, 236809 (2007).
  - [10] J. R. Schaibley, H. Yu, G. Clark, P. Rivera, J. S. Ross, K. L. Seyler, W. Yao, and X. Xu, *Nature Reviews Materials* **1** (2016).
  - [11] K. Behnia, *Nature Nanotechnology* **7**, 488 (2012).
  - [12] J. Lu, C. Qiu, M. Ke, and Z. Liu, *Physical Review Letters* **116**, 093901 (2016).
  - [13] J. Lu, C. Qiu, L. Ye, X. Fan, M. Ke, F. Zhang, and Z. Liu, *Nature Physics* **13**, 369 (2016).
  - [14] J.-W. Dong, X.-D. Chen, H. Zhu, Y. Wang, and X. Zhang, *Nature Materials* **16**, 298 (2017).
  - [15] X.-D. Chen, F.-L. Zhao, M. Chen, and J.-W. Dong, *Phys. Rev. B* **96** (2017), 10.1103/PhysRevB.96.020202.
  - [16] T. Ma and G. Shvets, *New J. Phys.* **18**, 025012 (2016).
  - [17] M. P. Makwana and R. V. Craster, *Physical Review B* **98**, 184105 (2018).
  - [18] M. Makwana and R. Craster, *Physical Review B* **98**, 235125 (2018).
  - [19] Z. Zhang, Y. Tian, Y. Cheng, Q. Wei, X. Liu, and J. Christensen, *Physical Review Applied* **9**, 034032 (2018).
  - [20] A. F. Morpurgo and F. Guinea, *Physical Review Letters* **97** (2006).
  - [21] R. K. Pal and M. Ruzzene, *New J. Phys.* **19**, 025001 (2017).

- [22] G. Carta, D. J. Colquitt, A. B. Movchan, N. V. Movchan, and I. S. Jones, *Philosophical Transactions of the Royal Society A: Mathematical, Physical and Engineering Sciences* **378**, 20190350 (2020).
- [23] K. Tang, M. P. Makwana, R. V. Craster, and P. Sebbah, arXiv:1910.08172 [cond-mat, physics:physics] (2019), arXiv: 1910.08172.
- [24] S. Brule, E. Javelaud, S. Enoch, and S. Guenneau, *Physical Review Letters* **112**, 133901 (2014).
- [25] A. Colombi, P. Roux, S. Guenneau, P. Gueguen, and R. Craster, *Scientific reports* **6**, 19238 (2016).
- [26] M. Miniaci, Krushynska, F. Bosia, and N. Pugno, *New J. Phys.* **18**, 083041 (2016).
- [27] G. Carta, I. Jones, N. N.V. Movchan, A. A.B. Movchan, and M. M.J. Nieves, *Proc. R. Soc. A* **473**, 20170136 (2017).
- [28] B. Ungureanu, S. Guenneau, Y. Achaoui, A. Diatta, M. Farhat, H. Hutridurga, R. Craster, S. Enoch, and S. Brule, *EPJ Appl. Metamat.* **6**, 18 (2019).
- [29] A. Colombi, D. Colquitt, P. Roux, S. Guenneau, and R. Craster, *Scientific reports* **6**, 27717 (2016).
- [30] K. Tsakmakidis, A. Boardman, and O. Hess, *Nature* **450**, 397 (2007).
- [31] A. Palermo, S. Kroedel, A. Marzani, and C. Daraio, *Scientific Reports* **6**, 39356 (2016).
- [32] R. Oulton, V. Sorger, D. Genov, D. Pile, and X. Zhang, *Nature Photonics* **2**, 496 (2008).
- [33] Q. Gan, Z. Fu, Y. Ding, and F. Bartoli, *Phys. Rev. Lett.* **100**, 256803 (2008).
- [34] P. Nagpal, N. Lindquist, S. Oh, and D. Norris, *Science* **325**, 594 (2009).
- [35] R. Boyd and D. Gauthier, *Science* **326**, 1074 (2009).
- [36] M. Sandtke and L. Kuipers, *Nature Photonics* **1**, 573 (2007).
- [37] C. Zhou, B. Yuan, Y. Cheng, and X. Liu, *Applied Physics Letters* **108**, 063501 (2016).
- [38] A. Colombi, P. Roux, and M. Rupin, *J. Acoust. Soc. Am.* **136**, EL192 (2014).
- [39] COMSOL, [www.comsol.com](http://www.comsol.com) (2018).
- [40] A. Diatta, M. Kadic, M. Wegener, and S. Guenneau, *Physical review B* **94**, 100105 (2016).
- [41] M. P. Makwana and G. Chaplain, *Scientific Reports* **9**, 18939 (2019).
- [42] M. Makwana, R. Craster, and S. Guenneau, *Optics Express* **27**, 16088 (2019).
- [43] M. P. Makwana, N. Laforge, R. V. Craster, G. Dupont, S. Guenneau, V. Laude, and M. Kadic, arXiv:1912.03232 [cond-mat, physics:physics] (2019), arXiv: 1912.03232.
- [44] T. Ochiai, *Physical Review B* **86** (2012).
- [45] K. Qian, D. J. Apigo, C. Prodan, Y. Barlas, and E. Prodan, arXiv:1803.08781 [cond-mat] (2018).
- [46] A. Colombi, V. Ageeva, R. Smith, A. Clare, R. Patel, M. Clark, D. Colquitt, P. Roux, S. Guenneau, and R. Craster, *Scientific Reports* **7**, 6750 (2017).
- [47] T. Antonakakis, R. V. Craster, and S. Guenneau, *New J. Phys* **15**, 103014 (2013).
- [48] M. Makwana, T. Antonakakis, B. Maling, S. Guenneau, and R. V. Craster, *SIAM Journal on Applied Mathematics* **76**, 1 (2016).
- [49] R. Wiltshaw, M. P. Makwana, and R. V. Craster, arXiv:2003.10876v2 [cond-mat, physics:physics] (2020), arXiv:2003.10876v2.
- [50] A. Colombi, D. Colquitt, P. Roux, S. Guenneau, and R. V. Craster, *Sci. Rep.* **6**, 27717 (2016).
- [51] P. Celli, B. Yousefzadeh, C. Daraio, and S. Gonella, *Applied Physics Letters* **114**, 091903 (2019).
- [52] Y. Achaoui, T. Antonakakis, S. Brule, R. Craster, S. Enoch, and S. Guenneau, *New Journal of Physics* **19**, 062022 (2017).
- [53] A. Palermo, S. Kroedel, K. Matlack, R. Zaccherini, V. Dertimanis, E. Chatzi, A. Marzani, and C. Daraio, *New Journal of Physics* **9**, 054026 (2018).
- [54] J. M. D. Ponti, A. Colombi, R. Ardito, F. Braghin, A. Corigliano, and R. V. Craster, *New Journal of Physics* **22**, 013013 (2020).

### Appendix A: Planar effects for an ungraded elastic plate

[41, 42] showed how by combining four structured domains a three-wave topological demultiplexer could be created using the  $C_{4v}$  model. [41] showed this beam splitting for the Kirchhoff-Love equation consisting of masses of infinitesimal radius. Similar effects were also achieved in the context of dielectric photonic crystals [42]. These effects are not contingent upon a variation in the depth of the medium and are therefore simpler to transpose to our full elastic medium comprised of judiciously rotated square boreholes. Fig. 7 shows a topological  $\pi/2$  bend and a three-way demultiplexer for a 3D elastic plate model. This elastic system is more challenging than the toy system found in [41] since all three elastic wave polarizations can couple at interfaces.

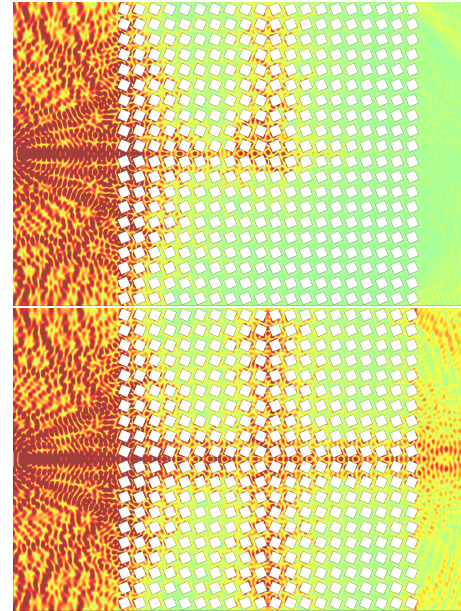


Figure 7: Top: Magnitude of out-of-plane component of displacement field showing propagation around a  $\pi/2$  bend at the interface between a single quadrant of squares oppositely orientated to the three remaining quadrants. Bottom: The three-way splitter ( $\omega/(2\pi) = 16.728Hz$ ), showing a typical wave pattern like a Saint-André cross, where the quadrants alternate in their relative rotation. In both panels the excitation is a point force polarized along the out-of-plane direction, which is located at the leftmost edge of the crystal. The computational domain shown is surrounded by 3D Perfectly Matched Layers.